Journal of Molecular Liquids 384 (2023) 122194

Contents lists available at ScienceDirect

Journal of Molecular Liquids

journal homepage: www.elsevier.com/locate/molliq

Colloidal suspensions of totally inorganic perovskites nanoparticles: A new photoluminescent emission in the near-IR

Mabel Rodríguez-Fernández [a], José Carlos Piñero [b], Rodrigo Alcántara [a], Javier Navas [a,*]

[a] Department of Physical Chemistry, University of Cádiz, E-11510 Puerto Real, Spain
[b] Department of Didactics (Area of Maths), University of Cádiz, E-11510 Puerto Real, Spain

ARTICLE INFO

Keywords:
Colloidal suspension
Perovskite materials
Luminescence
Nanomaterials

ABSTRACT

Luminescent materials have attracted great attention due to the amazing applications. In this sense, perovskite halide materials have shown promising luminescent properties which allows them to be useful in various applications such as LEDs, sensors. In this work, colloidal suspensions of $CsPbI_3$ and Pd-doped $CsPbI_3$ perovskite nanoparticles were prepared at different temperatures, and their structure and luminescence properties were characterized to analyse the effect of the synthesis temperature and the Pd-doping. With the increase of temperature, the main photoluminescence band of perovskite nanoparticles are slightly red-shifted. But the most amazing result is that the Pd-doped $CsPbI_3$ shows a new emission band at 877 nm under excitation at 785 nm. Therefore, this compound may be used as a highly sensitive luminescent sensor in several applications, such as in biosystems due to their emission in the first biological window under NIR excitation.

1. Introduction

Perovskite quantum dots (PQDs) have been something of a hot topic in the recent years due to their amazing properties, including high photoluminescence quantum yield, narrow bandwidth and tuneable photoluminescence, which make them promising materials for LEDs, lasers, solar cells or sensors [1]. Some of the most remarkable sensors whose working principle is based on the photoluminescence of quantum dots are those of ions, organic and inorganic compounds. Many materials have been tested as potential sensors based on photoluminescence properties, such as carbon dots [2], and mainly different rare earths ions used as dopants of different materials as Eu-doped zirconia [3], Eu-YVO_4 Nano-Phosphors [4], Sm^{3+}-doped $LiBaPO_4$ [5], or Eu^{3+}-doped YVO_4 [6]; or even organic compounds such as crushed roots of *Saccharum munja* grass [7]. In addition, halide-based perovskite materials are being widely studied. An example of the first kind of sensor is the one created by Yun Suk Huh et al. to detect products used to purify drinking water such as chlorine and iodine based on $CsPbBr_3$ perovskite quantum dots in a matrix of cellulose [8]. The importance of the detection of those ions lies in the fact that chlorine can form chloroform and other trihalomethanes that can produce cancer, and the lack or excess of iodine could also produce illnesses such as hyper- or hypothyroidism [8]. The working principle of this detector was a colorimetric and photoluminescence change produced through anionic exchange between the chlorine or iodine in the drinking water and the bromine of the perovskite quantum dots [8].

As mentioned above, PQD-based sensors of an inorganic molecule have been fabricated as well. For instance, Zhenyu Lin et al. developed an *in vivo* H_2S sensor based on nano-micelles of $CsPbBr_3$ encapsulated in a copolymer which worked on both living cells and zebrafishes [9]. The detection of this compound is based on the loss of the photoluminescence of the PQDs when the Pb^{+2} reacts with the S^{-2} to form black PbS [9]. Likewise, a specific H_2S sensor was fabricated, this being an important advance in biomedicine due to the fact that H_2S is a gasotransmitter in different biological functions such as vasorelaxation, angiogenesis, apoptosis, ageing and metabolism [10], and hence its detection would allow illnesses such as diabetes, Parkinson or Alzheimer to be diagnosed [9].

An example of a PQD-based biosensor of an organic molecule is the fluorescence resonance energy transfer (FRET) sensor to detect mycobacterium tuberculosis DNA developed by Xiaolan Yang et al [11]. This sensor is based on $CsPbBr_3$-COOH QDs conjugated with amino-terminal single-stranded DNA and MoS_2 nanosheets to bring about luminescence quenching [11]. In this way, when the QDs are attached to the MoS_2, their photoluminescence is quenched, but when the mycobacterium tuberculosis DNA hybridizes with the amino-terminal single–stranded

* Corresponding author.
E-mail address: javier.navas@uca.es (J. Navas).

https://doi.org/10.1016/j.molliq.2023.122194
Received 13 March 2023; Received in revised form 11 May 2023; Accepted 24 May 2023
Available online 29 May 2023

DNA, the QDs emit photoluminescence again as the double-stranded DNA cannot be adsorbed by MoS_2 nanosheets [11]. Those findings make PQDs relevant in the field of the biomedicine. Nevertheless, the most important contribution of PQDs in biomedicine is probably their use in the fabrication of PQD-based temperature sensors in luminescence nanothermometry. Luminescence nanothermometry (LNT) is a technique which uses nanothermometers based on materials whose photoluminescence emission is strongly temperature dependent, allowing the real-time nanoscale temperature to be determined [12]. Luminescence nanothermometry confers advantages such as having easy detection setups [13], high spatial resolution (<10 μm) in short acquisition times (<10 μs), high thermal resolution (0.1 K) [13] and high temperature sensitivity [13]. It is the only noncontact method providing the resolution and sensitivity required for effective *in vivo* and in vitro temperature measurements [14], and thus is capable of working even in harsh conditions such as in biological fluids [13].

Nevertheless, one of the main requirements of luminescent sensors for biological purposes is that they emit in the near-infrared (NIR) since depth of penetration decreases with photon energy [15]. Specifically, the materials used in those sensors should have an emission and excitation wavelength that fall in any of the three biological windows (BW). The first BW is in the 650–950 nm range, where the absorption of light by biological tissues and water is minimized [16]. The second BW is in the 1000–1350 nm range, where the Rayleigh and Mie scatterings are minimized [16]. Finally, the third BW is in the 1550–1870 nm range, where the absorbance and scattering by tissues decrease [16]. This allows a better depth of penetration of light through oxygenated blood and tissues that contain melanin [16].

Consequently, one of the limitations of the aforementioned sensors is that they do not emit in the NIR, meaning they are not ideal for *in vivo* applications. Specifically, they emit in the green range at 521.98 nm [8], 530 nm [9] and 522 nm [11], respectively, and the perovskite materials used in luminescent nanothermometers usually emit in the visible range as well [15]. Also, doped perovskite synthesized previously showed good interesting emission but not in the NIR range, for example Liu et al. reported Mn-doped $CsPbCl_3$ PQDs with emission at 580 nm [17], Kyun Ha et al. reported Mn-doped 2D perovskite based on Br showing an PL emission at about 620 nm [18], or Sn-doped $MAPbBr_3$ PQDs showed a slight shift towards high wavelength but with an emission by lower 520 nm [19]. Hence, it is necessary to synthesize new materials that emit in any of the three biological windows for their application on *in vivo* photoluminescence sensors.

In this paper, we prepared colloidal suspension of $CsPbI_3$ and Pd-doped $CsPbI_3$ perovskites synthesized through a hot-injection method. This composition was selected due to the fact that $CsPbX_3$ inorganic perovskites are more stable than their organic–inorganic halide counterparts such as $MAPbX_3$ or $FAPbX_3$ as the organic cation in the "A" position is volatile [20]. Among $CsPbX_3$ quantum dots, where X is Cl^-, Br^- or I^-, $CsPbI_3$ quantum dots have a red emission [21], its emission is red-shifted in comparison to the emission band of $CsPbBr_3$ (green emission) [22] and $CsPbCl_3$ (blue emission) [23]. It is, therefore, easier to tune their emission towards the NIR by doping. Furthermore, we synthesized the aforementioned samples at 130, 150 and 170 °C to explore the effect of the Pd-doping and the effect of the reaction temperature on their photoluminescence properties. We expected their photoluminescence to fall in the NIR thanks to the Pd-doping according to our previous work [24] and thus, that those quantum dots could be employed to fabricate *in vivo* sensors in the future. Thus, structural characterization, and the distribution of the elements in the perovskite materials was analyzed by TEM and EDS, and the optical properties were analyzed by means of UV–vis spectroscopy and steady-state and time-resolved photoluminescence measurements.

2. Experimental

2.1. Materials and reagents

Caesium carbonate (Cs_2CO_3, 99.5% trace metals basis), 1-octadecene (ODE for synthesis), oleic acid (OA, technical grade 90%), lead(II) iodide (PbI_2, 99%), palladium(II) iodide (PdI_2, ≥ 99.99%), oleylamine (OLA, technical grade 70%), toluene anhydrous (99.8%) were supplied by Sigma-Aldrich©.

2.2. Synthesis of Pd-doped $CsPbI_3$

Preparation of Cs-Oleate. The synthesis procedure followed was the method reported by Protesescu et al. [25]. In this method, 0.814 g of Cs_2CO_3, 40 mL of ODE and 2.5 mL of OA are loaded into 100 mL 3-neck flask, the mixture is dried for 1 h at 120 °C under vacuum and then heated on a hot plate to 150 °C under N_2 flow until the Cs_2CO_3 reacts with OA.

Synthesis of $CsPb_{1-x}Pd_xI_3$. The colloidal suspension of $CsPb_{1-x}Pd_xI_3$ nanoparticles (being × = 0 and 0.25) were obtained by using the hot-injection method [25]. In this method, 0.188 mmol of PbI_2 or a mixture of PbI_2 and PdI_2 in 5 mL of ODE was dried under vacuum for 1 h at 120 °C. Then, the flask containing the mixture was immersed in a silicone bath on a hot plate at this same temperature under N_2 flow. Then, 0.5 mL of OLA and 0.5 mL of OA were injected and when the salt was dissolved, the temperature was raised to 130 °C, 150 °C or 170 °C. Once this temperature was reached, 0.4 mL of Cs-oleate was injected, and then the flask was quickly immersed in an ice-water bath. Finally, the colloidal suspension was centrifuged at 7000 rpm for 10 min at 0 °C. After centrifuging, the supernatant was discarded and the precipitate was dispersed in anhydrous toluene for further analysis in the case of $CsPbI_3$. Nevertheless, we could not obtain precipitated nanocrystals for the doped samples, thus, the colloidal suspension of $CsPb_{0.75}Pd_{0.25}I_3$ nanoparticles in ODE was analysed in this case. As is discussed below, in some cases the size of the nanoparticles is enough small, thus QDs were obtained, but in other cases the sizes are higher than 10 nm, and we consider nanoparticles were synthesized.

2.3. Characterization of perovskite material synthesized

We employed transmission electron microscopy (TEM) to conduct the structural characterization of the synthesized perovskite materials. The TEM and HR-TEM images were acquired using a Talos F200s X Twin transmission electron microscope supplied by ThermoFisher Instruments® with an electron beam energy of 200 keV, an extraction voltage of 3900 V and an emission current of 65.1 μA. This instrument was also used to analyse the distributions of the elements in the samples using the high-angle annular dark-field scanning transmission electron microscopy (HAADF-STEM) image and the energy dispersive X-ray spectrometry (EDS) techniques. The optical properties of the synthesized perovskite materials were characterised using UV–Vis spectroscopy in absorbance mode. Our spectrometer, supplied by OceanOptics©, consists of a modular equipment with a DH-2000-BAL light source and USB2000 + spectrometer. The glass spectrophotometer cuvettes with a 10 mm light path (model 100–10-20) that we employed were supplied by Hellma Analytics™. The references we used to perform the optical measurements were anhydrous toluene in the case of $CsPbI_3$ and ODE in the case of the Pd-doped samples. Finally, the emission properties were analysed through photoluminescence spectroscopy. Steady-state photoluminescence spectra were recorded at room temperature with a Horiba© LabRAM HR Evolution Modular Raman spectrometer, which is suited for both Raman analysis and Photoluminescence and equipped with a Symphony II IR detector and a Sincerity visible detector both supplied by Horiba©. Different lasers were used as the excitation sources: a He-Cd laser emitting at 325 nm (model IK3201R-F 25 mW supplied by Kimmon Koha©); two DPSS (diode pumped solid state) lasers

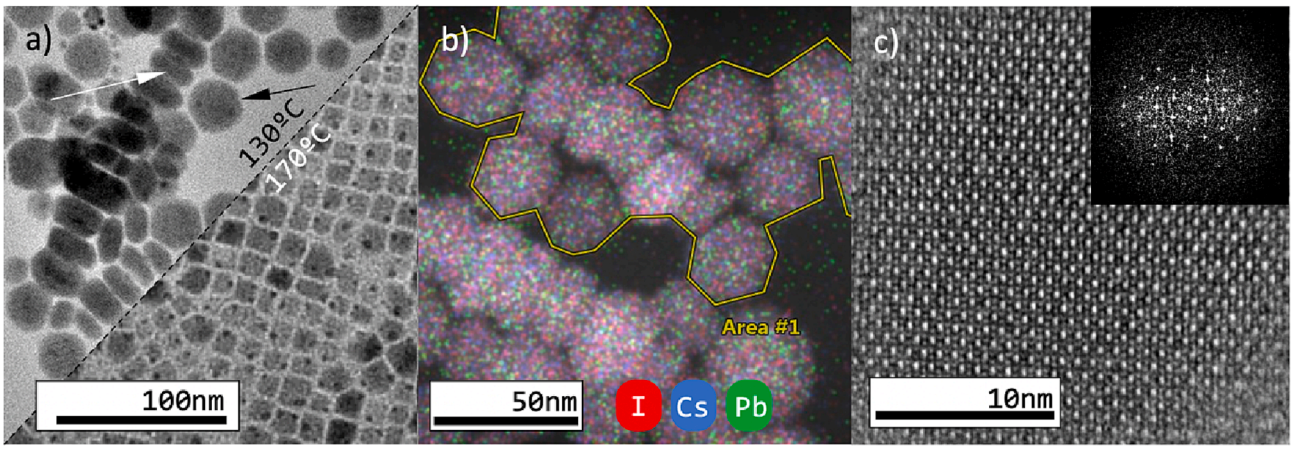

Fig. 1. (a) TEM BF micrography of $CsPbI_3$ nanoparticles synthesized at 130 °C and 170 °C, (b) superimposed plot of an HAADF image with an EDS map and (c) HREM micrography of a $CsPbI_3$ nanoparticle synthesized at 130 °C. SAED is presented as inset.

emitting at 473 and 532 nm with a power output of 100 mW supplied by Quantum models©; a He-Ne laser, supplied by Pacific LasertecTM, with an emission at 633 nm; and a Sacher Lasertechnik© laser emitting at 785 nm (model Pilot PC 500, power output: 100 mW).

Time-resolved photoluminescence measurements for estimating the lifetime of the emissions were measured using a DeltaFlex Modular Fluorescence Lifetime System supplied by Horiba© and employing a 467 nm nanoLED (pulse duration $<$ 200 ps) as the excitation source.

3. Results and discussion

3.1. Selected area diffraction (SAED) analysis

To explore the crystalline configuration of the different samples, TEM and EDS analysis were conducted using the 200 kV beam of a Talos F200X. Bright Field (BF) images were obtained and, as the nanoparticles were randomly oriented, a search for well-aligned nanoparticles (with respect to the incident beam) was performed.

Fig. 1a shows a BF image of $CsPbI_3$ nanoparticles synthesized at

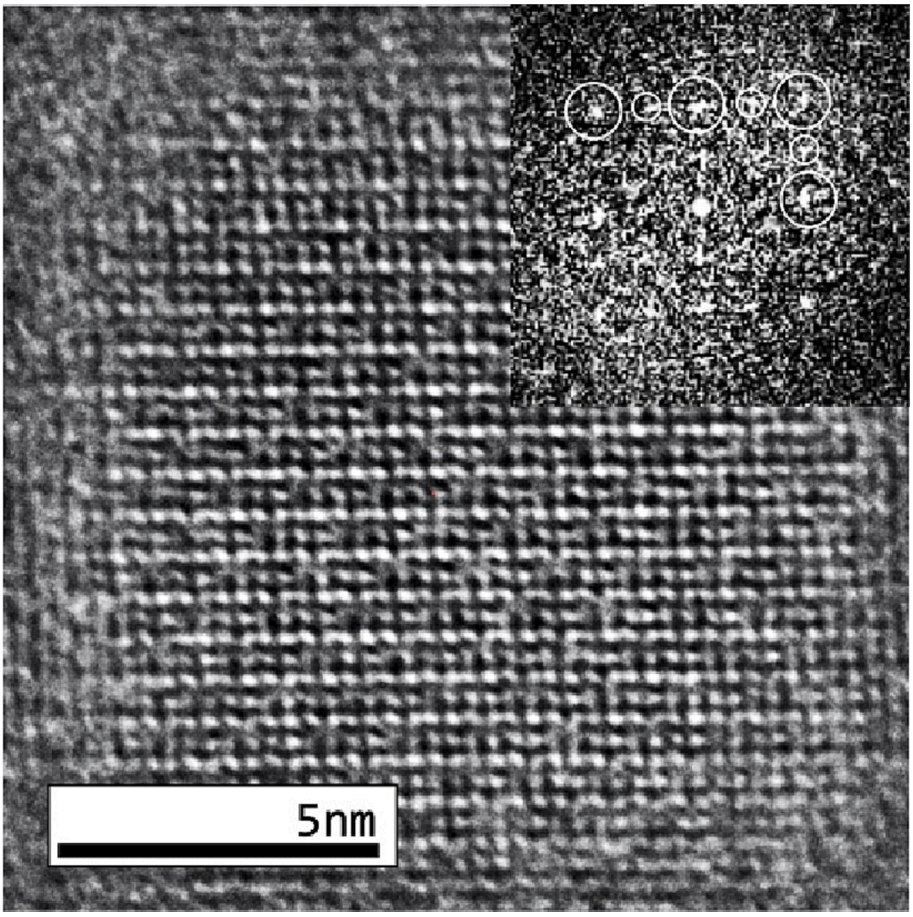

Fig. 2. HREM micrography of a $CsPbI_3$ nanoparticle synthesized at 170 °C. SAED data is presented as inset, where white circles are used to highlight diffraction spots.

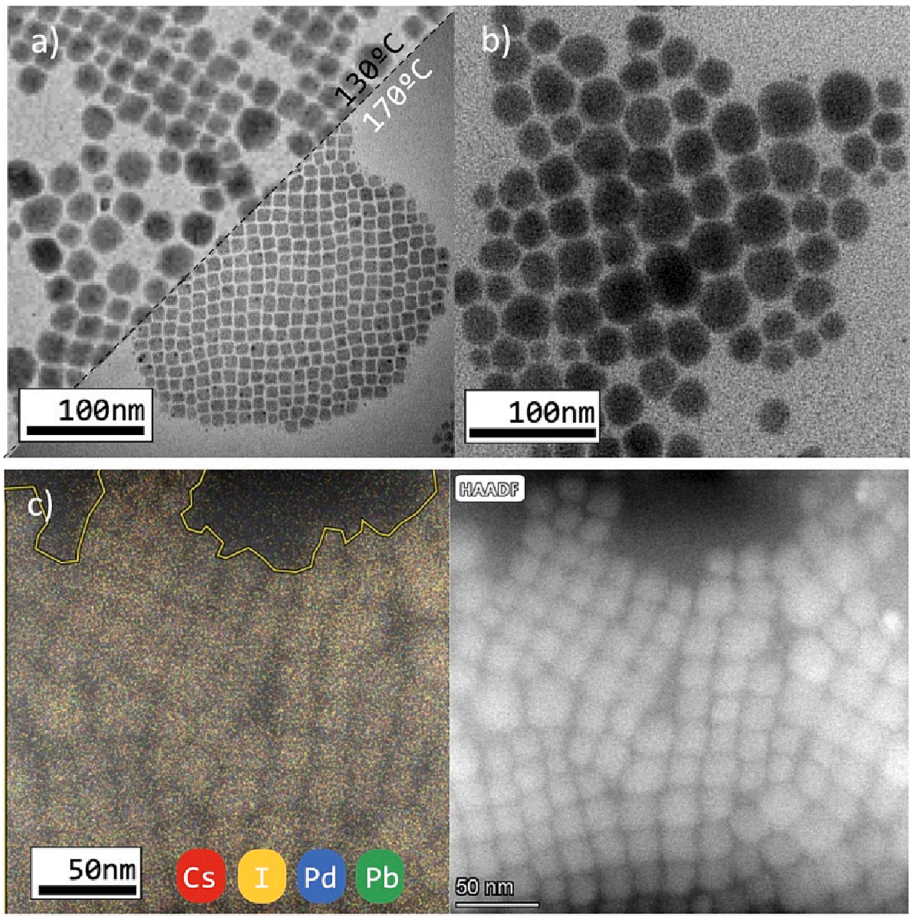

Fig. 3. (a) TEM BF micrography of Pd-doped $CsPbI_3$ nanoparticles synthesized at 130 °C, 170 °C and (b) 150 °C; c) superimposed plot of an HAADF image with an EDS map and the corresponding HAADF image.

130 °C. Hexagonal-shaped NPs are evidenced and highlighted with a black arrow. The mean apothem of such nanoparticles was found at about 16 nm, while the size of these nanoparticles varies slightly. On the other hand, some of the hexagonal nanoparticles are rotated enough to explore its thickness, which is about 14 nm. The morphology of these nanoparticles is clearly modified when synthesized at 170 °C, becoming cubes with edges of about 14 nm (see Fig. 1a). For the case of the nanoparticles synthesized at 150 °C, a mixture of both kinds of morphologies was detected, as is observed in Figure S1 In the supplementary Material. It is well-known the hot injection method allows to modify the size, morphology and stabilization of nanoparticle in controlled manner [26]. The shape of the quantum dots can be precisely controlled by adjusting synthesis parameters such as the ligand molecules used in their synthesis and the reaction temperature [27,28]. Furthermore, the method for synthesizing $CsPbX_3$ NCs can be divided into three parts: metal-oleic acid complex and X-ion release, $CsPbX_3$ seed nucleation and $CsPbX_3$ NC growth [29] The temperature varies the particle size and the high surface energy of the small particles in the colloidal system promotes their further growth, which is a phenomenon known as Ostwald ripening. Both the nucleation and the growth processes have important effects on the final particle size and morphology [26]. Therefore, this can explain the changes in the morphology with the reaction temperature of the nanoparticles synthesized in this work.

Regarding the composition and the element distribution on the nanoparticles, only the signals for Cs, Pb and I were observed, and no signal were found for any other element. In addition, EDS data shows a homogeneous distribution of the different composing elements, as is observed in Fig. 1b, where a representative EDS map for the sample synthesized at 130 °C is shown.

Finally, some of the nanoparticles showed an orientation suitable for a selected area diffraction pattern (SAED) study. This allows for HREM measurements and pole indexation, which allows the structure to be determined. In this regard, Fig. 1c presents HREM data of a hexagonal particle of the sample synthesized at 130 °C. Once the $[\bar{1}11]$ pole was determined, geometric distances were coincident to that of an orthorhombic $CsPbI_3$ system elongated on the C axis (particularly, a = 4.8 Å; b = 10.8 Å and c = 18.2 Å for the QD presented in Fig. 1c). The nanostructure of the particles changes with the synthesis temperature, as does their morphology. The minute size of the nanoparticles synthesized at 170 °C makes for a noisy SAED, which makes determining its crystalline system an extremely difficult task. The HREM data of a $CsPbI_3$ nanoparticle synthesized at 170 °C is provided in Fig. 2, which also presents SAED data as an inset. To guide the reader's eyes, white circles are positioned at the different diffraction spots of the SAED. The indexation of the [0 0 1] pole reveals a $CsPbI_3$ nanoparticle with a cubic structure axis (particularly, a = 6.3 Å; b = 6.6 Å and c = 6.7 Å for the nanoparticle presented on Fig. 2).

The morphology of the Pd-doped $CsPbI_3$ also depends on the synthesis temperature. Particularly, the sample synthesized at 130 °C shows a mixture of square and hexagonal-shaped nanoparticles (see Fig. 3a), the hexagonal particles being bigger than the square ones. In addition, full cubic nanoparticles were found at a synthesis temperature of 170 °C. In such cases cubic nanoparticles show an edge size of 10 nm. On the other hand, the QDs synthesized at 150 °C present a hexagonal, almost rounded morphology, probably due to the greater size of the particles (see Fig. 3b).

Concerning the composition and element distribution, the EDS data shows a homogeneous distribution of the different elements (see

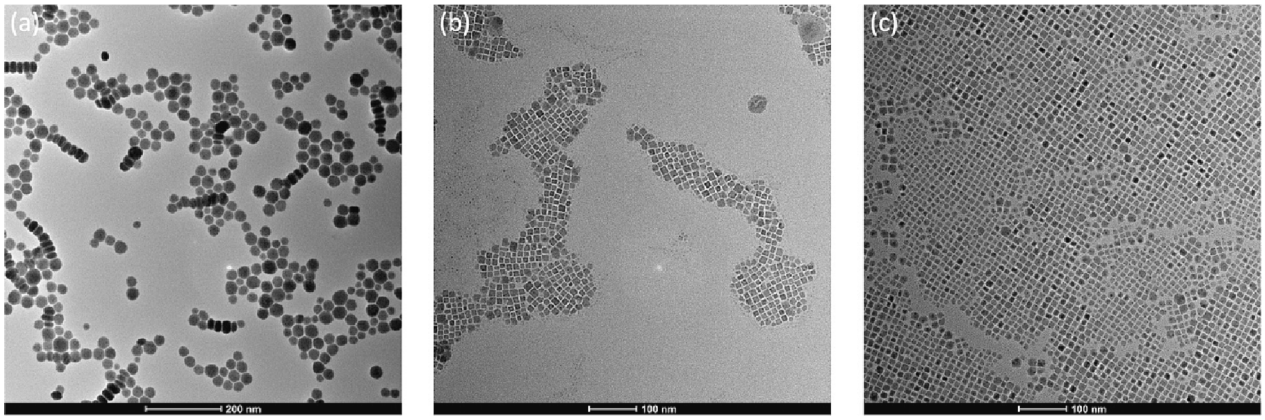

Fig. 4. TEM images of $CsPbI_3$ nanoparticles synthesized at 130 °C (a), 150 °C (b) and 170 °C (c).

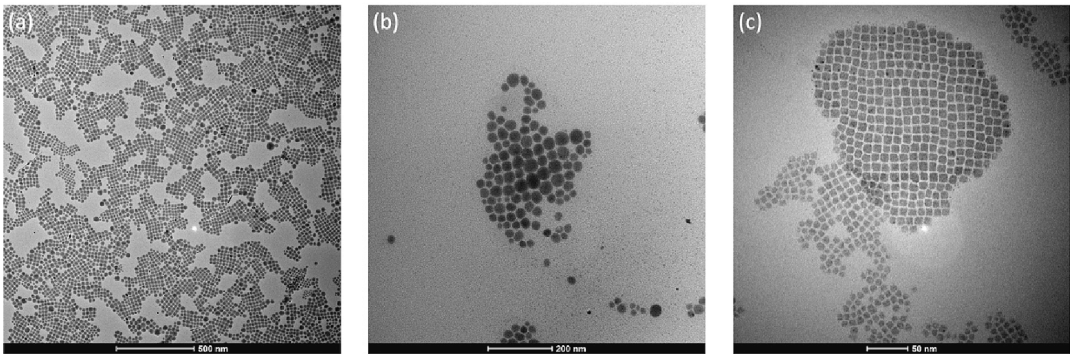

Fig. 5. TEM images of Pd-doped $CsPbI_3$ nanoparticles synthesized at 130 °C (a), 150 °C (b) and 170 °C (c).

Table 1
Average particle size of the synthesized samples.

T / °C	average size / nm	
	$CsPbI_3$	Pd-doped $CsPbI_3$
130 °C	28.9 ± 6.1 nm	19.4 ± 3.4 nm
150 °C	11.7 ± 2.0 nm	30.7 ± 7.2 nm
170 °C	12.2 ± 1.9 nm	9.4 ± 1.0 nm

Fig. 3c). No concentration or inhomogeneity of any element was detected, as in the case of $CsPbI_3$ nanoparticles. Furthermore, HREM-SAED measurements showed the same results in $CsPbI_3$ nanoparticles with respect to the changes of the nano crystalline structure, that is an orthorhombic structure for 130 °C and cubic for 170 °C.

We must emphasize that the SAED analysis is focused on specific particles, so the presence of particles with a different crystalline phase could be possible, as has been previously reported. For example, Akkerman et al. showed the formation of the non-luminescent Cs_4PbX_6 (X = Cl, Br, I) nanocrystals with hexagonal phase in perovskite QDs

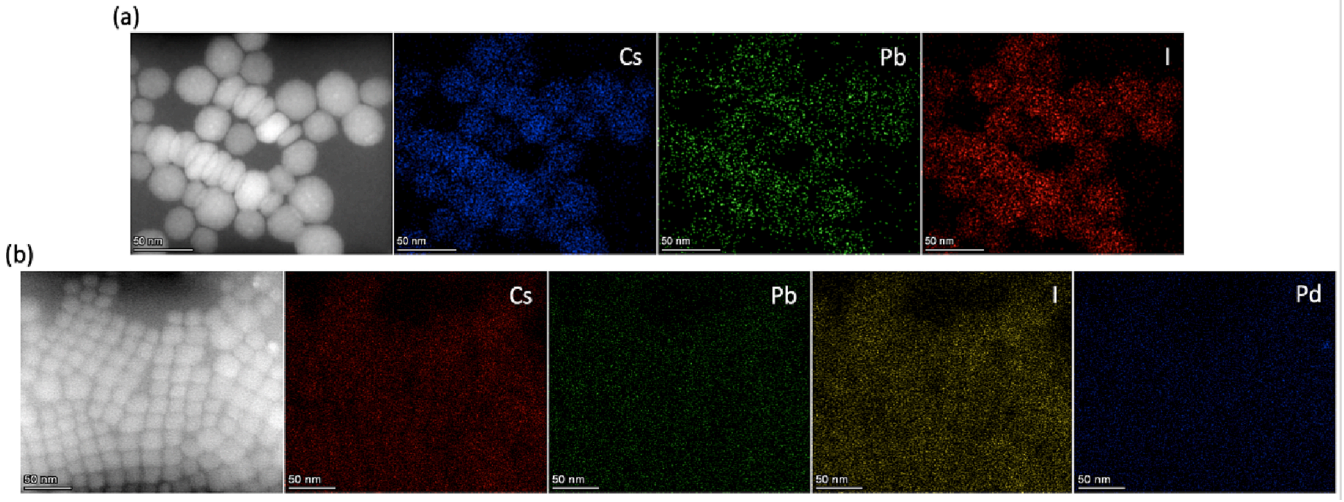

Fig. 6. HAADF-STEM image of $CsPbI_3$ nanoparticles (a) and the Pd-doped nanoparticles (b) and the corresponding EDS elemental mapping images of Cs, Pb, I and Pd elements for the sample synthesized at 130 °C.

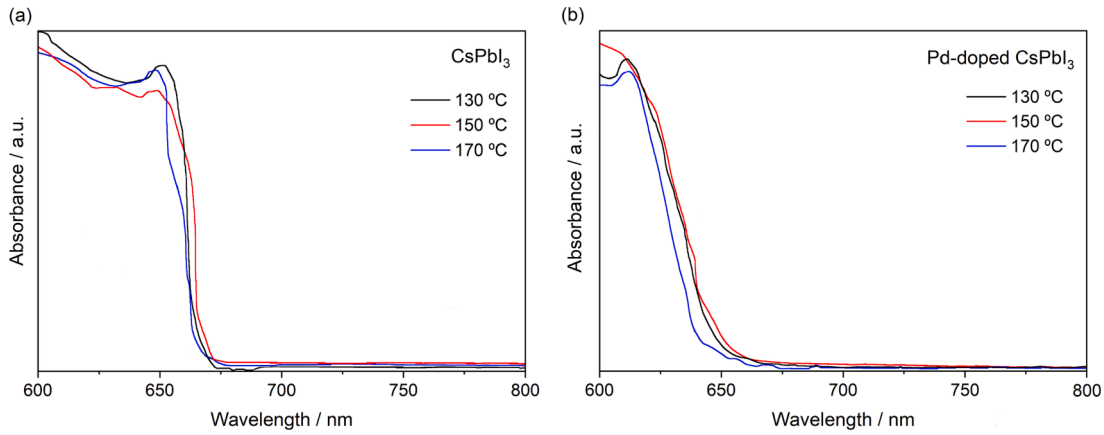

Fig. 7. UV–Vis spectra of $CsPbI_3$ nanoparticles (a) and Pd-doped $CsPbI_3$ (b) synthesized at different temperatures.

synthesis [30].

3.2. TEM analysis and size distribution

In addition, TEM images of the $CsPbI_3$ and Pd-doped $CsPbI_3$ nanoparticles illustrated in Figs. 4 and 5, respectively, show QDs which have the average diameters shown in Table 1, ranging from 11.7 to 28.9 nm in the case of the non-doped samples and from 9.4 to 30.7 nm in the case of the Pd-doped samples. The size distributions of the samples are shown in Figures S2 and S3 in the Supplementary Material.

The average particle size values show that there is a dependence of the particle size with the morphology analysed in the previous section. On the one hand, Pd-doped $CsPbI_3$ synthesized at 150 °C and pristine $CsPbI_3$ synthesized at 130 °C have a hexagonal morphology, which leads to bigger particle sizes. On the other hand, the samples synthesized at 170 °C have a cubic morphology, which results in smaller particle sizes. In the cases in which there is a mixture of hexagonal and cubic morphologies such as the Pd-doped $CsPbI_3$ synthesized at 130 °C and the $CsPbI_3$ nanoparticles synthesized at 150 °C, the average size values are between the typical values for hexagonal and cubic morphologies

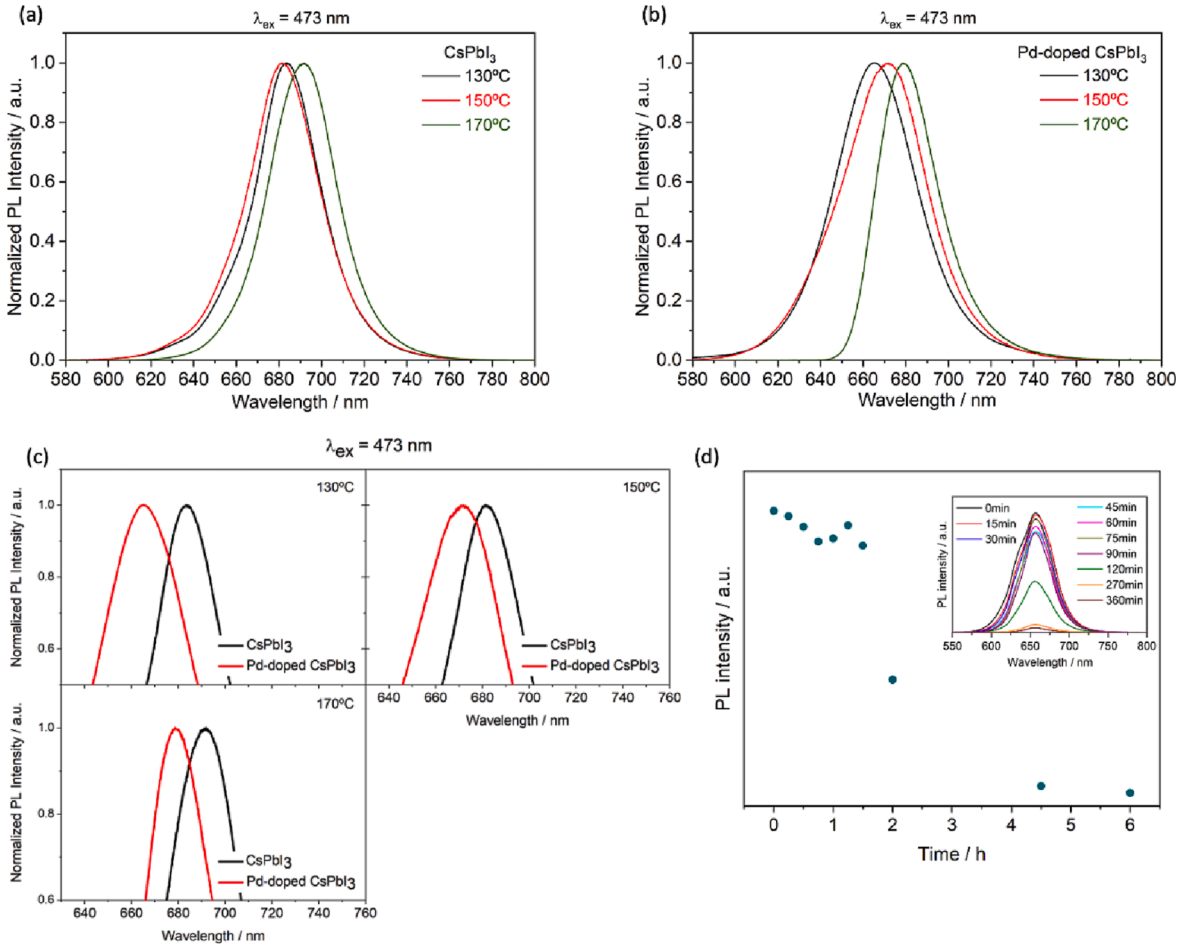

Fig. 8. Normalized PL spectra for $CsPbI_3$ (a) and Pd-doped $CsPbI_3$ (b) nanoparticles, and comparison between the undoped and doped samples for each synthesis temperature (c), and (d) stability analysis of the emission for a Pd-doped $CsPbBr_3$ perovskite sample synthesized at 130 °C.

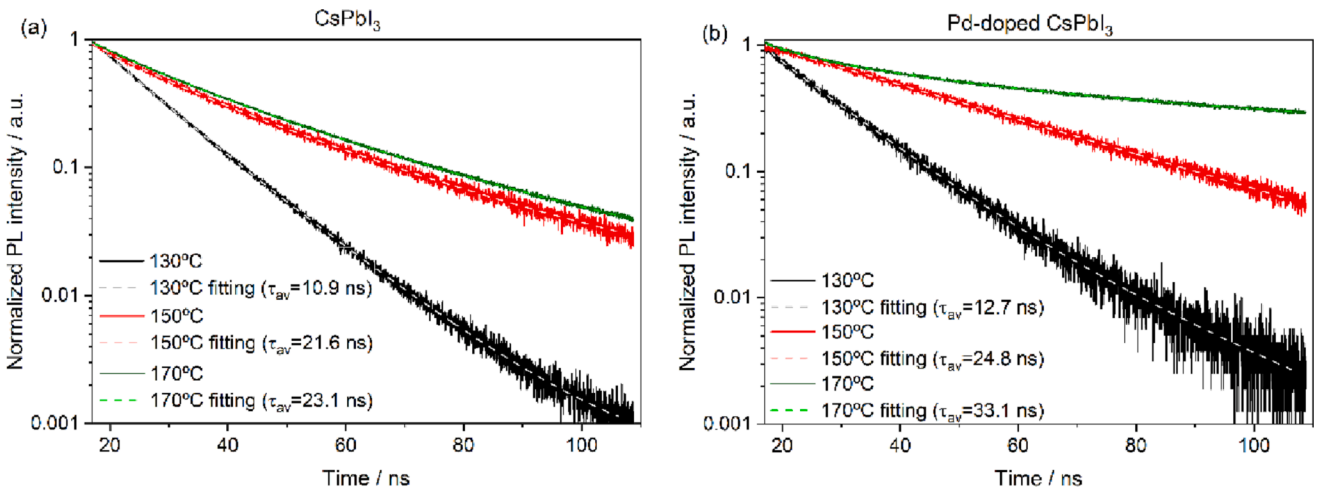

Fig. 9. Time-resolved PL decays and fitting curves for $CsPbI_3$ (a) and Pd-doped $CsPbI_3$ nanoparticles (b).

depending on the proportion of each morphology in the sample, bearing in mind that the number of particles analysed in several images is not close to the total particles in the samples synthesized. Thus, the average size does not show an increasing trend as the temperature rises, but rather it depends on the morphology.

3.3. HAADF-STEM and EDS

Also, the element distributions of the samples were studied using high-angle annular dark-field scanning transmission electron microscopy (HAADF-STEM) images coupled with energy dispersive X-ray spectrometry (EDS). Fig. 6 shows the HAADF-STEM image of $CsPbI_3$ nanoparticles and Pd-doped nanoparticles and the EDS elemental mapping images of Cs, Pb, I and Pd elements for the samples synthesized at 130 °C. In both the $CsPbI_3$ and Pd-doped $CsPbI_3$ QDs, the elements seem to be concentrated in certain areas, namely the brighter ones. In these areas, we can observe nanoparticles in the HAADF-STEM image. Furthermore, we can see that Pd and Pb are homogenously distributed in the sample, which evidences the Pd-doping of the samples.

3.4. UV–Vis spectroscopy

To further investigate the impact of the doping on the optical properties of the nanoparticles, an optical characterization was performed by means of UV–Vis spectroscopy. As shown in Fig. 7a, there is a band onset of about 665 nm of the pristine $CsPbI_3$ nanoparticles, and no significant shifts are observed in function of the temperature. Nevertheless, as Fig. 7b shows, doping leads to a blue shift of this absorption band, which shows an onset at about 635 nm. As will be discussed below, these results are coherent with the photoluminescence emission of the samples.

3.5. Photoluminescence spectroscopy

In addition, we performed photoluminescence measurements to investigate the effect of the synthesis temperature and Pd-doping on the emission properties of $CsPbI_3$ nanoparticles. Firstly, we studied the effect of the synthesis temperature. Fig. 8a shows the normalized spectra of pristine $CsPbI_3$ nanoparticles synthesized at 130, 150 and 170 °C under excitation at 473 nm. The band obtained at around 680 nm corresponds to the main emission of the $CsPbI_3$ nanocrystals [21]. The effect of the temperature on the main emission for the samples synthesized at 130 and 150 °C is not clear, but the band is slightly shifted to a longer wavelength when the $CsPbI_3$ nanoparticles are synthesized at 170 °C. In the case of the Pd-doped samples as well, we can see a progressive red-shift of the main emission band as the temperature is gradually increased, as shown in Fig. 8b. This trend is owing to the fact that the samples synthesized at 130 °C have an orthorhombic structure whilst those synthesized at 170 °C have a cubic structure. Therefore, the effect of the synthesis temperature in the emission band is a red-shift when temperature increases.

The second part of the study based on the steady-state PL measurements involved analysing the effect of Pd-doping on the emission properties. In Fig. 8c, the photoluminescence spectra of the undoped and Pd-doped samples are compared at each synthesis temperature obtained under excitation at 473 nm. Comparing those spectra shows that there is a blue-shift of the main emission band as we dope with Pd, which ranges between 9.7 and 18.2 nm depending on the synthesis temperature. Therefore, the effect of the Pd-doping in the emission band is a blue-shift. In addition, the stability of the perovskite synthesized was analyzed testing the emission for several hours. Fig. 8d shows the intensity of the emission, estimated as the area of the peak, up to 6 h after the synthesis for the Pd-doped $CsPbBr_3$ perovskite synthesized at 130 °C. A good stability of the emission is observed for 1.5 h.

3.6. Time-resolved photoluminescence spectroscopy

In Fig. 9, the decays and fitting curves of the different samples of the main emission at about 680 nm are represented. These PL decay curves were fitted through a tri-exponential decay function according to the details provided in the Supplementary Material in order to obtain average lifetime values. In general, an increase in the average lifetime was observed after doping with Pd. The decay plots obtained are fitted better to double or triple exponential function than a single one. This means there is fast decay and long decay components, which are associated with non-radiative and radiative recombination, indicating that there is a higher trap state density - thus a higher rate of non-radiative recombination - in undoped $CsPbI_3$ [31]. Moreover, the higher the synthesis temperature the higher the lifetime values; that is, when cubic structure and morphology is preferent, which is coherent with the literature because orthorhombic $CsPbI_3$ exhibits lifetime values lower than cubic $CsPbI_3$ [32]. Therefore, this means there is a higher rate of non-radiative recombination, that is, a higher trap state density, for the orthorhombic structure.

3.7. Emission in the IR zone

Finally, the most interesting results is that involving the excitation and emission in the near infrared. Photoluminescence spectra under excitation at 785 nm were also recorded to investigate the effectiveness of the Pd-doping of $CsPbI_3$ nanoparticles for obtaining emissions in the

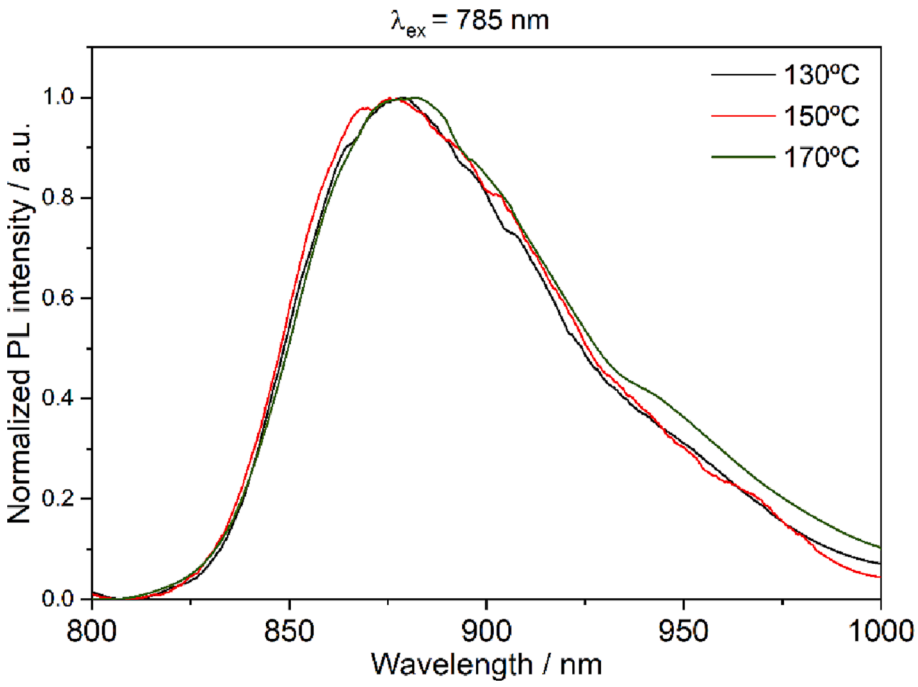

Fig. 10. Normalized photoluminescence spectra of Pd-doped $CsPbI_3$ nanoparticles synthesized at different temperatures obtained after excitation of the samples with a 785 nm laser.

NIR. The Pd-doped samples presented a band at around 877 nm under excitation with the NIR laser (see Fig. 10), with a quantum yield of about 9.5%. On the contrary, the undoped samples did not show any photoluminescence band. This is due to the interactions Pd-I, which affects to the band structure in Pd-doped perovskite [18]. Thus, these results allow us to conclude that Pd-doping is an effective way to obtain NIR emission, and that Pd-doped $CsPbI_3$ QDs could be used as *in vivo* sensors in biological systems thanks to their emission in the first biological window under excitation with an NIR laser.

4. Conclusions

In this work, we prepared colloidal suspensions of $CsPbI_3$ and Pd-doped $CsPbI_3$ nanoparticles synthesized at different temperatures (130, 150 and 170 °C) through the hot-injection method. SAED analysis confirms the presence of a perovskite structure, obtaining orthorhombic and cubic structures for respective synthesis temperatures of 130 and 170 °C. Furthermore, the morphology of the particles - cubic or hexagonal - depends on the synthesis temperature, that is on the size of the nanoparticles. The particle size was obtained by the analysis of TEM images. We found that their size depends on the morphology, the hexagonal particles being bigger than the cubic ones. In addition, we studied the effect of Pd-doping and the synthesis temperature on the optical properties of nanoparticles. The results of this study show a shift towards lower wavelength values of the main PL band as the temperature decreases and after doping with Pd. However, the most outstanding result is the NIR emission at 877 nm under excitation with a 785 nm laser found for the Pd-doped samples, which makes them a good candidate as a material for *in vivo* biosensors.

CRediT authorship contribution statement

Mabel Rodríguez-Fernández: Formal analysis, Investigation, Methodology, Writing – original draft. **José Carlos Piñero:** Methodology. **Rodrigo Alcántara:** Formal analysis, Validation. **Javier Navas:** Funding acquisition, Project administration, Supervision, Writing – review & editing.

Declaration of Competing Interest

The authors declare that they have no known competing financial interests or personal relationships that could have appeared to influence the work reported in this paper.

Data availability

The authors do not have permission to share data.

Acknowledgements

This work was supported by the Ministerio de Universidades del Gobierno de España [grant number FPU19/02336]; and the Ministerio de Ciencia e Innovación del Gobierno de España [grant number TED2021-132518B-I00].

Data availability

The raw/processed data required to reproduce these findings cannot be shared at this time due to legal or ethical reasons.

Appendix A. Supplementary material

Supplementary data to this article can be found online at https://doi.org/10.1016/j.molliq.2023.122194.

References

[1] H. Chen, A. Guo, X. Gu, M. Feng, Highly luminescent $CsPbX_3$ (X=Cl, Br, I) perovskite nanocrystals with tunable photoluminescence properties, J. Alloy. Compd. 789 (2019) 392, https://doi.org/10.1016/j.jallcom.2019.03.049.
[2] A. Kumar, I. Kumar, A.K. Gathania, Synthesis, characterization and potential sensing application of carbon dots synthesized via the hydrothermal treatment of cow milk, Sci. Rep.-Uk 12 (2022) 22495, https://doi.org/10.1038/s41598-022-26906-4.
[3] I. Kumar, A. Kumar, A.K. Gathania, Activation of zirconia nanophosphors with Eu3 +to demonstrate multifunctional optical applications, Mater. Chem. Phys. 292 (2022), 126846, https://doi.org/10.1016/j.matchemphys.2022.126846.

[4] S. Thakur, A.K. Gathania, Fluorescence study of Eu-YVO4 nano-phosphors as a function of calcination temperature and excitation wavelengths, J. Fluoresc. 25 (2015) 657, https://doi.org/10.1007/s10895-015-1551-z.
[5] I. Kumar, A.K. Gathania, Photoluminescence and quenching study of the Sm3+-doped LiBaPO4 phosphor, J. Mater. Sci.-Mater. El. 33 (2022) 328, https://doi.org/10.1007/s10854-021-07301-7.
[6] S. Thakur, A.K. Gathania, Optical properties of YVO4: Eu3+ nano-phosphors at different europium concentrations, Indian J. Phys. 89 (2015) 973, https://doi.org/10.1007/s12648-015-0670-3.
[7] S. Thakur, A.K. Gathania, Structural and optical studies on the crushed roots of Saccharum munja grass: a new low cost red phosphor source for optical applications, Indian J. Phys. 91 (2017) 623, https://doi.org/10.1007/s12648-017-0967-5.
[8] B. Park, S.-M. Kang, G.-W. Lee, C.H. Kwak, M. Rethinasabapathy, Y.S. Huh, Fabrication of CsPbBr 3 perovskite quantum dots/cellulose-based colorimetric sensor: dual-responsive on-site detection of chloride and iodide ions, Ind. Eng. Chem. Res. 59 (2020) 793, https://doi.org/10.1021/acs.iecr.9b05946.
[9] F. Luo, S. Li, L. Cui, Y. Zu, Y. Chen, D. Huang, Z. Weng, Z. Lin, Biocompatible perovskite quantum dots with superior water resistance enable long-term monitoring of the H_2S level in vivo, Nanoscale 13 (2021) 14297, https://doi.org/10.1039/D1NR02248B.
[10] V.K. Pal, P. Bandyopadhyay, A. Singh, Hydrogen sulfide in physiology and pathogenesis of bacteria and viruses, Int. Union Biochem. Mol. Biol. Life 70 (2018) 393, https://doi.org/10.1002/iub.1740.
[11] X. Jiang, H. Zeng, C. Duan, Q. Hu, Q. Wu, Y. Yu, X. Yang, One-pot synthesis of stable and functional hydrophilic CsPbBr 3 perovskite quantum dots for "turn-on" fluorescence detection of Mycobacterium tuberculosis, Dalton Trans. 51 (2022) 3581, https://doi.org/10.1039/D1DT03624F.
[12] B. del Rosal, E. Ximendes, U. Rocha, D. Jaque, In vivo luminescence nanothermometry: from materials to applications, Adv. Opt. Mater. 5 (2017) 1600508, https://doi.org/10.1002/adom.201600508.
[13] A. Nexha, J.J. Carvajal, M.C. Pujol, F. Díaza, M. Aguiló, Lanthanide doped luminescence nanothermometers in the biological windows: strategies and applications, Nanoscale 13 (2021) 7913, https://doi.org/10.1039/D0NR09150B.
[14] C. Matuszewska, K. Elzbieciak-Piecka, L. Marciniak, Transition metal ion-based nanocrystalline luminescent thermometry in $SrTiO_3$:Ni^{2+}, E^{r3}+ nanocrystals operating in the second optical window of biological tissues, J. Phys. Chem. C 123 (2019) 18646–18653, https://doi.org/10.1021/acs.jpcc.9b04002.
[15] A. Bednarkiewicz, L. Marciniak, L.D. Carlos, D. Jaque, Standardizing luminescence nanothermometry for biomedical applications, Nanoscale 12 (2020) 14405, https://doi.org/10.1039/D0NR03568H.
[16] O. Savchuk, J.J.C. Marti, C. Cascales, P. Haro-Gonzalez, F. Sanz-Rodríguez, M. Aguilo, F. Diaz, Bifunctional Tm^{3+}, Y^{b3}+:GdV_O4@Si_O2 core-shell nanoparticles in HeLa cells: upconversion luminescence nanothermometry in the first biological window and biolabelling in the visible, Nanomaterials 10 (2020) 993, https://doi.org/10.3390/nano10050993.
[17] H. Liu, Z. Wu, J. Shao, D. Yao, H. Gao, Y. Liu, W. Yu, H. Zhang, B. Yang, CsPbxMn1−xCl3 perovskite quantum dots with high Mn substitution ratio, ACS Nano 11 (2017) 2239, https://doi.org/10.1021/acsnano.6b08747.
[18] S. Kyun Ha, W. Shcherbakov-Wu, E.R. Powers, W. Paritmongkol, W.A. Tisdale, Power-dependent photoluminescence efficiency in manganese-doped 2D HybridPerovskite nanoplatelets, ACS Nano 15 (2021) 20527, https://doi.org/10.1021/acsnano.1c09103.
[19] A. Mehta, J. Im, B. Hyung Kim, H. Min, R. Nie, S. Il Seok, Stabilization of lead−tin-alloyed inorganic−organic halide perovskite quantum dots, ACS Nano 12 (2018) 12129, https://doi.org/10.1021/acsnano.8b05478.
[20] J. Zhang, P.G. Hodes, P.Z. Jin, P.S.F. Liu, All-inorganic $CsPbX_3$ perovskite solar cells: progress and prospects, Angew. Chem. Int. Ed. 58 (2019) 15596, https://doi.org/10.1002/anie.201901081.
[21] F. Liu, Y. Zhang, C. Ding, S. Kobayashi, T. Izuishi, N. Nakazawa, T. Toyoda, T. Ohta, S. Hayase, T. Minemoto, K. Yoshino, S. Dai, Q. Shen, Highly luminescent phase-stable cspbi$_3$ perovskite quantum dots achieving near 100% absolute photoluminescence quantum yield, ACS Nano 11 (2017) 10373, https://doi.org/10.1021/acsnano.7b05442.
[22] O.-H.-C. Cheng, T. Qiao, M. Sheldon, D.H. Son, Size- and temperature-dependent photoluminescence spectra of strongly confined CsPbBr 3 quantum dots, Nanoscale 12 (2020) 13113, https://doi.org/10.1039/D0NR02711A.
[23] D. Parobek, B.J. Roman, Y. Dong, H. Jin, E. Lee, M. Sheldon, D.H. Son, Exciton-to-dopant energy transfer in Mn-doped Cesium lead halide perovskite nanocrystals, Nano Lett. 16 (2016) 7376, https://doi.org/10.1021/acs.nanolett.6b02772.
[24] J. Navas, A. Sánchez-Coronilla, J.J. Gallardo, J.C. Piñero, D. De los Santos, E. I. Martín, N.C. Hernández, R. Alcántara, C. Fernández-Lorenzo, J. Martín-Calleja, The impact of Pd on the light harvesting in hybrid organic-inorganic perovskite for solar cells, Nano Energy 34 (2017) 141, https://doi.org/10.1016/j.nanoen.2017.02.035.
[25] L. Protesescu, S. Yakunin, M.I. Bodnarchuk, F. Krieg, R. Caputo, C.H. Hendon, R. X. Yang, A. Walsh, M.V. Kovalenko, Nanocrystals of Cesium lead halide perovskites ($CsPbX_3$, X = Cl, Br, and I): novel optoelectronic materials showing bright emission with wide color gamut, Nano Lett. 15 (2015) 3692, https://doi.org/10.1021/nl5048779.
[26] R.K. Ratnesh, Hot injection blended tunable CdS quantum dots for production of blue LED and a selective detection of Cu2+ ions in aqueous medium, Opt Laser Technol 116 (2019) 103, https://doi.org/10.1016/j.optlastec.2019.03.001.
[27] M. Alizadeh-Ghodsi, M. Pourhassan-Moghaddam, A. Zavari-Nematabad, B. Walker, N. Annabi, A. Akbarzadeh, State-of-the-art and trends in synthesis, properties, and application of quantum dots-based nanomaterials, Part. Part. Syst. Char. 36 (2019) 1800302, https://doi.org/10.1002/ppsc.201800302.
[28] S. Ananthakumar, J.R. Kumar, S.M. Babu, Cesium lead halide (CsPbX3, X = Cl, Br, I) perovskite quantum dots-synthesis, properties, and applications: a review of their present status, J. Photon Energy 6 (2016), 042001, https://doi.org/10.1117/1.Jpe.6.042001.
[29] Z.H. Wu, J. Wei, Y.N. Sun, J. Wu, Y.F. Hou, P. Wang, N.P. Wang, Z.F. Zhao, Air-stable all-inorganic perovskite quantum dot inks for multicolor patterns and white LEDs, J. Mater. Sci. 54 (2019) 6917, https://doi.org/10.1007/s10853-019-03382-2.
[30] Q.A. Akkerman, S. Park, E. Radicchi, F. Nunzi, E. Mosconi, F. De Angelis, R. Brescia, P. Rastogi, M. Prato, L. Manna, Nearly monodisperse insulator Cs4PbX6 (X = Cl, Br, I) nanocrystals, their mixed halide compositions, and their transformation into CsPbX3 nanocrystals, Nano Lett. 17 (2017) 1924, https://doi.org/10.1021/acs.nanolett.6b05262.
[31] Y.-K. Wang, F. Yuan, Y. Dong, J.-Y. Li, A. Johnston, B. Chen, M.I. Saidaminov, C. Zhou, X. Zheng, Y. Hou, K. Bertens, H. Ebe, D. Ma, Z. Deng, S. Yuan, R. Chen, L. K. Sagar, J. Liu, J. Fan, P. Li, X. Li, Y. Gao, M.-K. Fung, Z.-H. Lu, O.M. Bakr, L.-S. Liao, E.H. Sargent, All-inorganic quantum-dot LEDs based on a phase-stabilized α-$CsPbI_3$ perovskite, Angew. Chem. 60 (2021) 16164, https://doi.org/10.1002/anie.202104812.
[32] B. Li, Y. Zhang, L. Fu, T. Yu, S. Zhou, L. Zhang, L. Yin, Surface passivation engineering strategy to fully-inorganic cubic $CsPbI_3$ perovskites for high-performance solar cells, Nat. Commun. 9 (2018) 1076, https://doi.org/10.1038/s41467-018-03169-0.